Linearized pipe flow to Reynolds number 10^7

Á. Meseguer, L.N. Trefethen *

Computing Laboratory, Oxford University, Wolfson Building, Parks Road, Oxford OX1 3QD, UK

Received 4 May 2002; accepted 16 January 2003

Abstract

A Fourier–Chebyshev Petrov–Galerkin spectral method is described for high-accuracy computation of linearized dynamics for flow in an infinite circular pipe. Our code is unusual in being based on solenoidal velocity variables and in being written in MATLAB. Systematic studies are presented of the dependence of eigenvalues, transient growth factors, and other quantities on the axial and azimuthal wave numbers and the Reynolds number R for R ranging from 10^2 to the idealized (physically unrealizable) value 10^7. Implications for transition to turbulence are considered in the light of recent theoretical results of S.J. Chapman.

1. Introduction

Three classical incompressible shear flows have received attention in connection with the phenomenon of "subcritical" or "nonmodal" or "bypass" transition to turbulence [9,28]. Plane Poiseuille and plane Couette channel flows are the most accessible to theoretical analysis and numerical computation and have been the subject of numerous studies [4,6,12,14,17,23,24,31]. Pipe flow (also known as pipe Poiseuille or Hagen–Poiseuille flow) is the most accessible to laboratory experiments [7,8,35]. It was in the context of flow in a pipe that Reynolds in 1883 identified the basic problem of this field: when and how do high-speed flows undergo transition from the laminar state to more complicated states such as puffs, slugs, and turbulence [26]?

The present paper concerns the numerical simulation of pipe flow. It is a product of an ongoing collaboration between ourselves, working on the computer, and Prof. Tom Mullin of the University of Manchester, working in the laboratory. A general aim of this collaboration is, by developing numerical and experimental methods in tandem, to help narrow the gap between two communities and literatures that have not communicated as well as they might have. Specifically, we aim to focus on some of the principal mechanisms by which small perturbations in high speed flow may grow as they flow downstream and develop into complicated structures associated with turbulence. Our focus is on the elucidation of key mechanisms involved in transition, not on fully developed turbulence.

With these aims in mind, and with an acute awareness of the continuing advance of desktop and laptop computers, we have written a high accuracy Petrov–Galerkin spectral code for pipe flow in MATLAB. In principle we are thus engaged in direct numerical simulation (DNS) of the Navier–Stokes equations. On the computers available today, fully resolved DNS demands multiple processors, and MATLAB is not competitive with Fortran or C for such computations. On a single processor, however, a well-designed MATLAB code may run slower than the equivalent Fortran or C code by only a modest factor equivalent to, say, a year or two of technological advance in hardware. In exchange for this modest cost in machine speed one gets a great gain in human efficiency, flexibility, and compactness and portability of code, since MATLAB is a high-level language with the principal operations of linear algebra and fast Fourier transform built in, as well as powerful graphics. For example, our linearized pipe flow code is listed as a brief appendix to this paper; one would hardly do such a thing with Fortran or C. Today, MATLAB is a good vehicle for coarsely resolved pipe flows. In a few years, it will be good for medium resolution too.

This paper is devoted to linear effects, with nonlinear interactions deferred to a subsequent publication. One reason for this is that the main features of our methods of discretization, which are not standard, can be described in the linear context. Another is that in view especially of a recent paper of Chapman [6], certain questions related to the nonlinear problem of transition to turbulence can be examined in the linear case. In this paper we first describe our discretization, then present various numerical results that go beyond those reported previously, including asymptotic expressions for various quantities as $R \to \infty$. At the end we consider some implications in the light of Chapman's analysis.

Previous numerical simulations of (nonlinear) pipe flow have included works of Boberg and Brosa [3], Komminaho and Johansson [13], O'Sullivan and Breuer [21], Priymak and Miyazaki [22], Shan et al. [29], Zhang et al. [36], and Zikanov [37]. In addition, various previous authors have simulated linearized pipe flow [2,16,27,32]. Our methods could be summarized as a solenoidal scheme for the pipe of the sort proposed by Leonard and Wray [16], but using Chebyshev rather than Jacobi polynomials, so that the FFT is applicable, which entails a Petrov–Galerkin rather than Galerkin formulation, as described by Moser et al. for other geometries [20] (see also Section 7.3.3 of [5]); and with regularity conditions at the center of the pipe imposed in the manner of Priymak and Miyazaki [22,33]. Some further details of our work can be found in [18].

2. Pipe flow equations and laminar flow solution

In an infinite circular pipe of radius a, we consider the flow of an incompressible Newtonian fluid with dynamic viscosity μ and density ρ driven by an external constant axial pressure gradient $\mathrm{d}p_0/\mathrm{d}z = -\Pi$. Let $V = V(t)$ denote the three-dimensional velocity field vector at a given time t; we use the symbol V rather than the more usual $\mathbf{v}$ to make a distinction that can be carried over to the computer program from the three components u, v, w to be introduced below. The Navier–Stokes equations are

$$V_t + (V \cdot \nabla)V = \rho^{-1}(\Pi\hat{z} - \nabla p + \mu\Delta V), \tag{1}$$

where the subscript denotes a partial derivative, $\hat{z}$ is the unit vector in the axial direction, and p is the pressure relative to p_0; we supplement (1) with the zero-divergence equation

$$\nabla \cdot V = 0 \tag{2}$$

and the no-slip condition $V = 0$ on the boundary. The dimensions of each term in (1) are $(\text{length})/(\text{time})^2$. We nondimensionalize by selecting space, time, and mass scales $[L] = a$, $[T] = 4\mu/\Pi a$, and $[M] = \rho a^3$, respectively, and redefining accordingly the space and time variables and the dependent variables V and p.

Eq. (1) becomes

$$\frac{[L]}{[T]^2} V_t + \frac{[L]}{[T]^2}(V \cdot \nabla)V = \rho^{-1}\Pi\hat{z} - \rho^{-1}\frac{[M]}{[L]^2[T]^2}\nabla p + \frac{\rho^{-1}\mu}{[T][L]}\Delta V,$$

or, after multiplying through by $[T]^2/[L]$,

$$V_t + (V \cdot \nabla)V = \frac{[T]^2}{[L]}\rho^{-1}\Pi\hat{z} - \rho^{-1}\frac{[M]}{[L]^3}\nabla p + \frac{\rho^{-1}\mu[T]}{[L]^2}\Delta V,$$

which simplifies to

$$V_t + (V \cdot \nabla)V = \frac{16\mu^2}{\Pi a^3 \rho}\hat{z} - \nabla p + \frac{4\mu^2}{\Pi a^3 \rho}\Delta V.$$

If we define the nondimensional *Reynolds number* by

$$R = \frac{\Pi a^3 \rho}{4\mu^2}, \tag{3}$$

then the equation becomes

$$V_t + (V \cdot \nabla)V = 4R^{-1}\hat{z} - \nabla p + R^{-1}\Delta V. \tag{4}$$

These are the *nondimensional Navier–Stokes equations for flow in a pipe*.

We can express (4) explicitly in terms of cylindrical coordinates r (radial), θ (azimuthal), and z (axial). If u, v, and w denote the radial, azimuthal, and axial components of V, respectively, then (4) takes the form [15]

$$u_t + uu_r + r^{-1}vu_\theta + wu_z - r^{-1}v^2 = -p_r + R^{-1}(u_{rr} + r^{-1}u_r + r^{-2}u_{\theta\theta} + u_{zz} - 2r^{-2}v_\theta - r^{-2}u), \tag{5}$$

$$v_t + uv_r + r^{-1}vv_\theta + wv_z + r^{-1}uv = -r^{-1}p_\theta + R^{-1}(v_{rr} + r^{-1}v_r + r^{-2}v_{\theta\theta} + v_{zz} + 2r^{-2}u_\theta - r^{-2}v), \tag{6}$$

$$w_t + uw_r + r^{-1}vw_\theta + ww_z = 4R^{-1} - p_z + R^{-1}(w_{rr} = r^{-1}w_r + r^{-2}w_{\theta\theta} + w_{zz}), \tag{7}$$

and Eq. (2) in cylindrical coordinates is

$$u_r + r^{-1}v_\theta + w_z + r^{-1}u = 0. \tag{8}$$

The boundary condition now takes the form

$$u = v = w = 0 \quad \text{for } r = 1. \tag{9}$$

It is readily seen that independently of R, there is a steady solution to (5)–(9), the *laminar flow*, consisting of pure axisymmetric axial motion:

$$p = -\Pi z + \text{const.}, \qquad u = 0, \quad v = 0, \quad w = 1 - r^2. \tag{10}$$

Note that in our nondimensional variables, the laminar flow has speed 1 at the centerline; this was the reason for including the factor 4 in the definition of $[T]$. In other words, an equivalent definition to (3) would be

$$R = \frac{a\rho}{\mu}U_{\text{CL}},$$

where $U_{\text{CL}} = [L]/[T] = \Pi a^2/4\mu$ is the velocity of the laminar flow at the centerline in dimensional units.

3. Linearization and reduction to Fourier modes

For numerical solution of the Navier–Stokes equations, it is convenient to take as dependent variables the perturbation of the velocity field from the laminar solution. The result are equations in which the velocity components interact both linearly and quadratically.

Our concern in this paper is the linearized problem in which only infinitesimal perturbations from the laminar flow are considered. This is achieved by setting quadratic terms with respect to such perturbations to zero. Let $\bar{p} = $ const., $\bar{u} = 0$, $\bar{v} = 0$, and $\bar{w} = 1 - r^2$ denote the pressure and velocity variables of (10). Let p, u, v, and w denote the perturbations of these quantities from their laminar values. Then the linearizations of (5)–(7) take the form

$$u_t + \bar{w}u_z = -p_r + R^{-1}(u_{rr} + r^{-1}u_r + r^{-2}u_{\theta\theta} + u_{zz} - 2r^{-2}v_\theta - r^{-2}u), \tag{11}$$

$$v_t + \bar{w}v_z = -r^{-1}p_\theta + R^{-1}(v_{rr} + r^{-1}v_r + r^{-2}v_{\theta\theta} + v_{zz} + 2r^{-2}u_\theta - r^{-2}v), \tag{12}$$

$$w_t + u\bar{w}_r + \bar{w}w_z = -p_z + R^{-1}(w_{rr} + r^{-1}w_r + r^{-2}w_{\theta\theta} + w_{zz}), \tag{13}$$

and (8) looks the same as before,

$$u_r + r^{-1}v_\theta + w_z + r^{-1}u = 0. \tag{14}$$

Eqs. (11)–(14) are linear, and the cylindrical domain is periodic in θ and unbounded in z. It follows that all solutions to these equations can be expressed as superpositions of complex Fourier modes of the form

$$V(r,\theta,z,t) = e^{i(n\theta+kz)}V(r,t), \qquad p(r,\theta,z,t) = e^{i(n\theta+kz)}p(r,t) \tag{15}$$

for appropriate functions $V(r,t)$ and $p(r,t)$, where $n \in Z$ and $k \in R$. Moreover, the functions corresponding to different k or n are orthogonal, so there are no pitfalls in making use of such a decomposition. Let the r, θ, and z components of $V(r,t)$ be denoted by $u(r,t), v(r,t), w(r,t)$, respectively. Introducing (15) into (11)–(13) gives the equations

$$u_t = -p_r + R^{-1}(u_{rr} + r^{-1}u_r - n^2r^{-2}u - k^2u - 2inr^{-2}v - r^{-2}u) - ik\bar{w}u, \tag{16}$$

$$v_t = -r^{-1}p_\theta + R^{-1}(v_{rr} + r^{-1}v_r - n^2r^{-2}v - k^2v + 2inr^{-2}u - r^{-2}v) - ik\bar{w}v, \tag{17}$$

$$w_t = -p_z + R^{-1}(w_{rr} + r^{-1}w_r - n^2r^{-2}w - k^2w) - u\bar{w}_r - ik\bar{w}w \tag{18}$$

and (14) becomes

$$u_r + inr^{-1}v + ikw + r^{-1}u = 0. \tag{19}$$

4. Solenoidal Petrov–Galerkin discretization

The numerical method we have chosen for (16)–(19) is adapted from work in the early 1980s by Leonard and Wray [16] and Moser et al. [20]; see Section 7.3.3 of [5] for a summary. If (16)–(18) are a system of linear partial differential equations of the form $V_t = \mathscr{L}V$, then the weak form of the same system is $(V_t, W) = (\mathscr{L}V, W)$ for all W in a suitable space of test functions, where $(\cdot, \cdot)$ denotes the inner product over the spatial domain. In our problem, because of (19), V is solenoidal (i.e., divergence-free) and zero at the boundary. It follows that one may restrict attention to test functions W with the same properties, since if

$(V_1, W) = (V_2, W)$ for all solenoidal functions W that are zero at the boundary, then in particular $(V_1, V_1 - V_2) = (V_2, V_1 - V_2)$, i.e., $(V_1 - V_2, V_1 - V_2) = 0$, implying $V_1 = V_2$. Now by (2.4), the terms involving the pressure in $(\mathcal{L}V, W)$ are of the form $(\nabla p, W)$. Since $W = 0$ at the boundary, integration by parts implies that this is the same as $-(p, \nabla \cdot W)$, which is zero since $\nabla \cdot W = 0$. Thus by restricting attention to solenoidal velocity fields we have eliminated the pressure variable and the incompressibility condition (19) and reduced (16)–(19) to the weak form

$$(V_t, W) = (\mathcal{L}V, W) \qquad \forall W,$$

with $\mathcal{L}V$ defined by its three components

$$(\mathcal{L}V)_1 = R^{-1}(u_{rr} + r^{-1}u_r - n^2r^{-2}u - k^2u - 2inr^{-2}v - r^{-2}u) - ik\bar{w}u, \tag{20}$$

$$(\mathcal{L}V)_2 = R^{-1}(v_{rr} + r^{-1}v_r - n^2r^{-2}v - k^2v + 2inr^{-2}u - r^{-2}v) - ik\bar{w}v, \tag{21}$$

$$(\mathcal{L}V)_3 = R^{-1}(w_{rr} + r^{-1}w_r - n^2r^{-2}w - k^2w) - u\bar{w}_r - ik\bar{w}w. \tag{22}$$

For our numerical method, we will approximate V and W in finite-dimensional spaces of solenoidal functions. This would be difficult in arbitrary geometries, but is feasible in the simple geometry of a pipe. In what follows, we define

$$h_m(r) = (l - r^2)T_{2m}(r), \quad g_m(r) = (1 - r^2)^2 T_{2m}(r), \tag{23}$$

where T_{2m} is the Chebyshev polynomial of degree $2m$. We begin with V, distinguishing two cases depending on whether n is zero or nonzero.

Case $n = 0$. If $n = 0$, the solenoidal condition (19) becomes $u_r + r^{-1}u + ikw = 0$, implying that v is arbitrary but u and w are related by a condition that we may write as

$$D_+u + ikw = 0,$$

where D_+ is an abbreviation for $d/dr + r^{-1}$. In addition, continuity of the velocity field at $r = 0$ implies that u (radial) and v (azimuthal) must be zero there, whereas w (axial) can be nonzero. Likewise, by (19), the no-slip conditions imply u_r at $r = 1$. A suitable basis for functions satisfying these conditions is the set of functions

$$V_m^{(1)} = \begin{pmatrix} 0 \\ rh_m(r) \\ 0 \end{pmatrix}, \qquad V_m^{(2)} = \begin{pmatrix} -ikrg_m(r) \\ 0 \\ D_+[rg_m(r)] \end{pmatrix} \tag{24}$$

for $m = 0, 1, \ldots$, except that if $k = 0$, the third component of $V_m^{(2)}$ is replaced by $h_m(r)$.

Case $n \neq 0$. Here we take

$$V_m^{(1)} = \begin{pmatrix} -inr^{|n|-1}g_m(r) \\ D[r^{|n|}g_m(r)] \\ 0 \end{pmatrix}, \qquad V_m^{(2)} = \begin{pmatrix} 0 \\ -ikr^{|n|+1}h_m(r) \\ inr^{|n|}h_m(r) \end{pmatrix}. \tag{25}$$

Mathematically speaking, the factors of i in $V_m^{(2)}$ could be dispensed with, but we leave them in so that the basis functions have a desirable symmetry property: if k and n are negated, each basis function is replaced by its complex conjugate.

So much for the bases for the functions V. For the functions W, we could take the same bases. However, the resulting matrices would be dense, whereas they can be made to be banded if we choose $W_m^{(1)}$ and $W_m^{(2)}$ instead as follows:

Case n = 0.

$$W_m^{(1)} = \frac{1}{\sqrt{1-r^2}} \begin{pmatrix} 0 \\ h_m(r) \\ 0 \end{pmatrix}, \tag{26}$$

$$W_m^{(2)} = \frac{1}{\sqrt{1-r^2}} \begin{pmatrix} ikr^2 g_m(r) \\ 0 \\ D_+[r^2 g_m(r)] + r^3 h_m(r) \end{pmatrix}, \tag{27}$$

except that if $k = 0$, the third component of $W_m^{(2)}$ is replaced by $r h_m(r)$.

Case n ≠ 0. Define $s = 0$ if n is even; 1 if n is odd. The basis functions are

$$W_m^{(1)} = \frac{1}{\sqrt{1-r^2}} \begin{pmatrix} inr^s g_m(r) \\ D[r^{1+s} g_m(r)] + r^{2+s} h_m(r) \\ 0 \end{pmatrix}, \tag{28}$$

$$W_m^{(2)} = \frac{1}{\sqrt{1-r^2}} \begin{pmatrix} 0 \\ -ikr^{2+s} h_m(r) \\ inr^{1+s} h_m(r) rg \end{pmatrix}, \tag{29}$$

except that if $k = 0$ and n is odd, the third component of $W_m^{(2)}$ is replaced by $inh_m(r)$.

For further details about (25)–(29). and for more comprehensive information about our numerical method, including the analysis of regularity of solutions at the coordinate singularity $r = 0$, see [18]. Also see Appendix A, which lists the code used to compute all the numerical results below.

5. Eigenvalues

We now begin to summarize some of the results of our computations. In doing this we have several purposes. One is to record detailed enough results for assessment of the efficiency of our methods and for future comparison by others. A second is to report various asymptotic expressions for behavior as $R \to \infty$ that have not been investigated before. A third is to review some of the main physical phenomena of linearized pipe flow, which in combination with quadratic nonlinear couplings generate turbulence and other flow effects. We shall see that even this purely linear analysis has implications for transition.

For much of the discussion we focus on two pairs of Fourier parameters:

$$n = 1, \ k = 0 \quad \text{and} \quad n = 1, \ k = 1. \tag{30}$$

Of course, many more wave numbers than these combine to make up an actual flow. These two choices, nevertheless, represent two of the most important components of pipe flow dynamics: streamwise-independent or more briefly just "streamwise" structures ($k = 0$), with space and time scales $O(R)$, and streamwise-dependent structures ($k \neq 0$), with space and time scales $O(R^{1/2})$ or $O(R^{1/3})$. We remind the reader that although n is necessarily an integer, k can be any real number and has just been chosen to be an integer for simplicity.

We begin with eigenvalues. Fig. 1 shows some of the rightmost eigenvalues in the complex plane of the evolution operator $\mathscr{L}$ for the parameters (30) with $R = 10^3$, 10^4, and 10^5. The values of M used were 8, 24, 74 for $k = 0$ and 18, 57, 180 for $k = 1$ for the three Reynolds numbers: the corresponding complex matrix

eigenvalue problems are of dimensions 18, 50, 150 and 38, 116, 362. We found these to be the minimum values that give results converged to high accuracy, and each computation takes less than a second on our workstation, except for the one with $M = 150$.

Looking qualitatively at the figures, the first thing we note is that in the streamwise case $k = 0$, all the eigenvalues are real. They cluster close to the origin as $R \to \infty$, revealing that certain streamwise modes are only slightly damped for large R. For $k = 1$, on the other hand, we have the three branches of eigenvalues well known in pipe and channel flows and discussed, for example, in [9] and [28]. The eigenvalues λ with $\operatorname{Im}\lambda \approx 0$ correspond to wall modes, concentrated near the pipe wall and with low phase speed. The eigenvalues λ with $\operatorname{Im}\lambda \approx 1$ correspond to center modes, concentrated near the center of the pipe and with phase speed close to 1. The remaining eigenvalues, extending in a line with $\operatorname{Im}\lambda \approx 2/3$ towards $-\infty$ in the complex plane, correspond to global modes with phase speed $\approx 2/3$.

For $R = 10^5$, the expected line of eigenvalues with $\operatorname{Im}\lambda \approx 2/3$ does not appear in the last panel of Fig. 1: instead we see a cloud of eigenvalues bounded by two cluster curves. These results are due to rounding errors, and they do not improve if M is increased. Mathematically speaking, they are incorrect, but this is a case where the correct results would be no more meaningful physically than the incorrect ones, for as we shall discuss in the next section, the eigenvalues shown, and indeed all other numbers in the same general area of the complex plane, are exact eigenvalues of an operator $\mathscr{L} + \Delta\mathscr{L}$ with $\|\Delta\mathscr{L}\| < 10^{-10}$. In other words all of these numbers are ϵ-pseudo-eigenvalues of $\mathscr{L}$ for a value of ϵ far smaller the precision of any laboratory experiment.

Table 1 lists the rightmost eigenvalues for the three cases of interest. We believe that these numbers are correct in all but possibly the last of the 10 digits given. Fig. 2 shows details of convergence of the rightmost center and wall eigenvalues for $n = 1$ and $k = 1$. (For $k = 0$ the convergence is so fast that $M = 5$ suffices for 10-digit precision for all rightmost eigenvalues.) In verifying our code we have, among other tests, compared certain numerical quantities against previously published results in [16] and [22]. In [32] one can also find plots of eigenvalues in which results for the Fourier modes n and k are not separated but superimposed in a single image; this corresponds to the spectrum of the whole linear operator $\mathscr{L}$ rather than to various of its Fourier projections.

It is interesting to compare the asymptotic behavior of these three different kinds of eigenvalues, a subject analyzed theoretically for channel flows (without numerical constants) in [6]. For the streamwise case $n = 1$ and $k = 0$, the rightmost eigenvalue approaches 0 as $R \to \infty$ almost exactly in proportion to R^{-1}. An approximation accurate to many digits is

$$\lambda_{\text{streamwise}} \approx -14.6819706 R^{-1}. \tag{31}$$

The R^{-1} scaling implies that energy in this mode will decay on a time scale $\mathrm{O}(R)$.

For $n = k = 1$, there are two eigenvalues of special interest. For the rightmost center mode eigenvalue, a good approximation is

$$\lambda_{\text{center}} \approx \mathrm{i} - (2.28058 + 4.85519\mathrm{i}) R^{-1/2} + (0.92 + 0.32\mathrm{i}) R^{-1}. \tag{32}$$

The imaginary part ≈ 1 reflects the wave speed ≈ 1, and the real part $\mathrm{O}(R^{-1/2})$ indicates decay on a time scale $\mathrm{O}(R^{1/2})$. For the rightmost wall mode eigenvalue, a good approximation is

$$\lambda_{\text{wall}} \approx (-1.680 + 6.548\mathrm{i}) R^{-1/3} + 14.3 R^{-2/3} - 450\mathrm{i} R^{-1}. \tag{33}$$

Evidently these waves propagate with phase speed $\mathrm{O}(R^{1/3})$ and decay on a time scale $\mathrm{O}(R^{1/3})$. This difference between $R^{-1/2}$ behavior for the center modes and $R^{-1/3}$ behavior for the wall modes has been known since work by Pekeris (1948), Corcos and Sellars (1959), and Gill (1965); see [9] for a summary and references. These authors' analytical estimates concerned the axisymmetric case $n = 0$; our estimates (32) and (33) represent extensions to nonaxisymmetric flows.

The approximations (31)–(33) are shown graphically in Fig. 3. Fig. 4 shows stream functions for these three modes for $R = 3000$.
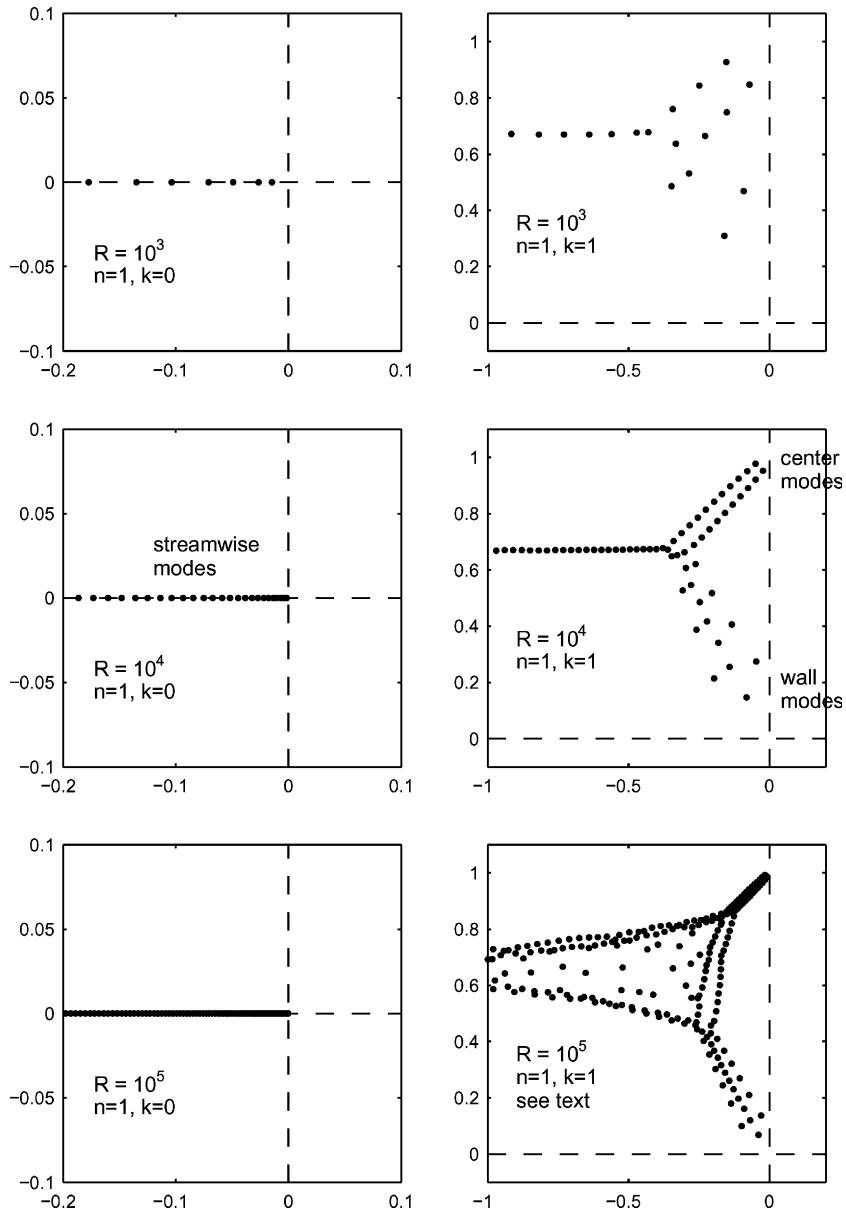
Fig. 1. Numerically computed eigenvalues in the complex plane for $n = 1$ and $k = 0, 1$ with $R = 10^3, 10^4, 10^5$. The first five plots are correct to plotting accuracy. The last one is not correct, but it is a correct figure for an operator perturbed by an amount less than one part in 10^{-10}; see Fig. 9.

6. Transient effects and pseudospectra

We now move to computational results which, unlike eigenvalues and eigenmodes, are norm-dependent—and, on the whole, more significant physically. The norm in question is the standard "energy" measure of perturbations used in studies of this kind, the root-mean-square velocity perturbation from

Table 1
Rightmost eigenvalues in the complex plane

R	$n = 1$, $k = 0$	$n = 1$, $k = 1$, center mode	$n = 1$, $k = 1$, wall mode
10^2	−0.1468197064	—	−0.1471366653 + 0.5725629712i
10^3	−0.0146819706	−0.0708640053 + 0.8467498288i	−0.0911426036 + 0.4691428789i
10^4	−0.0014681971	−0.0227049146 + 0.9514811947i	−0.0472321996 + 0.2737887093i
10^5	−0.0001468197	−0.0072023080 + 0.9846498286i	−0.0292364601 + 0.1372143077i
10^6	−0.0000146820	−0.0022796480 + 0.9951451356i	−0.0153380019 + 0.0649631475i
10^7	−0.0000014682	−0.0007210913 + 0.9984646856i	−0.0074895687 + 0.0303389812i

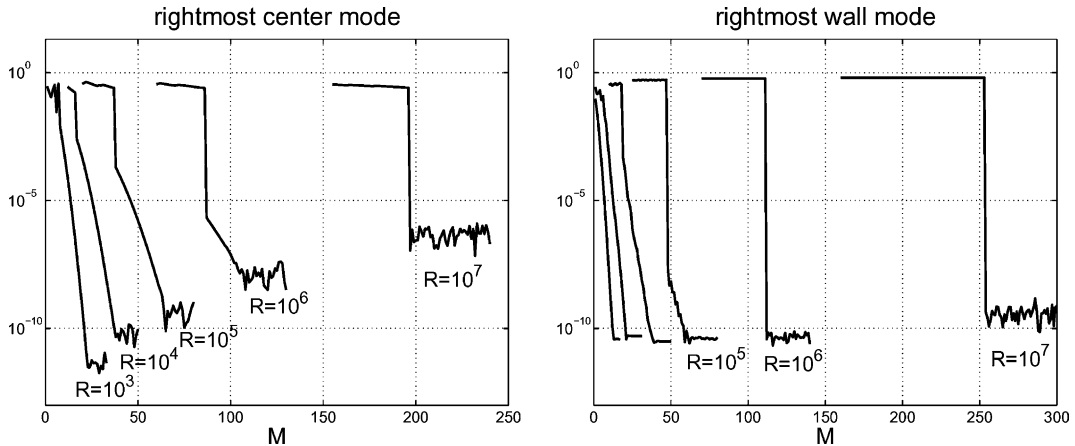Fig. 2. Error in the rightmost center and wall mode eigenvalues as a function of discretization parameter M, for $n = 0$ and $k = 1$ and Reynolds numbers $R = 10^2, 10^3, \ldots, 10^7$. The matrix dimension is $2M + 2$, The convergence is spectral in each case until limited by rounding errors. As $R \to \infty$, the value of M needed to resolve these modes is about $R^{1/3}$.

laminar. Because the operators and matrices involved are nonnormal, this norm of a perturbation is not simply proportional to the vector norm of its coefficients in an expansion in eigenvectors. Instead, to calculate the norm correctly one must weight these coefficients by a nondiagonal matrix multiplication, as discussed for example in Appendix A of [25]. We do not spell out the details, but they can be found in [18] and are encoded in our MATLAB programs in Appendix A.

The most basic quantitative effect to look for is transient growth of three-dimensional ($n \neq 0$) disturbances, whose importance in shear flows was highlighted around 1990 by Boberg and Brosa [3], Butler and Farrell [4], Gustavsson [12], and Reddy and Henningson [23], among others. Fig. 5 shows the maximum possible transient growth as a function of t for various values of n with $k = 0$ and $k = 1$ (cf. Fig. 4 of [27], Fig. 6 of [32], and Fig. 4 of [2]). In other words, it shows the operator norm $\| \exp(t\mathscr{L}) \|$ as a function of t. For the streamwise modes with $k = 0$, the growth is substantial: amplification by a factor $\mathrm{O}(R)$ on a time scale $\mathrm{O}(R)$. For the nonstreamwise modes with $k \neq 0$, there is still a transient effect, but it is smaller: amplification $\mathrm{O}(R^{1/3})$ on a time scale $\mathrm{O}(R^{1/3})$. These exponents cannot be seen in Fig. 5, since just a single value of R is shown, but they appear in Fig. 6, which displays the dependence on R on a log–log scale. In this figure and elsewhere, t_{opt} denotes the value of t at which $\| \exp(t\mathscr{L}) \|$ is maximized.

Table 2 lists the numbers underlying Fig. 6 for values of R equal to powers of 10. By analyzing these and other such numbers we estimate for $k = 0$,

$$\sup_{t<0} \| \exp(t\mathscr{L}) \| \approx R/117.7 \quad \text{attained at } t \approx R/20.42, \tag{34}$$
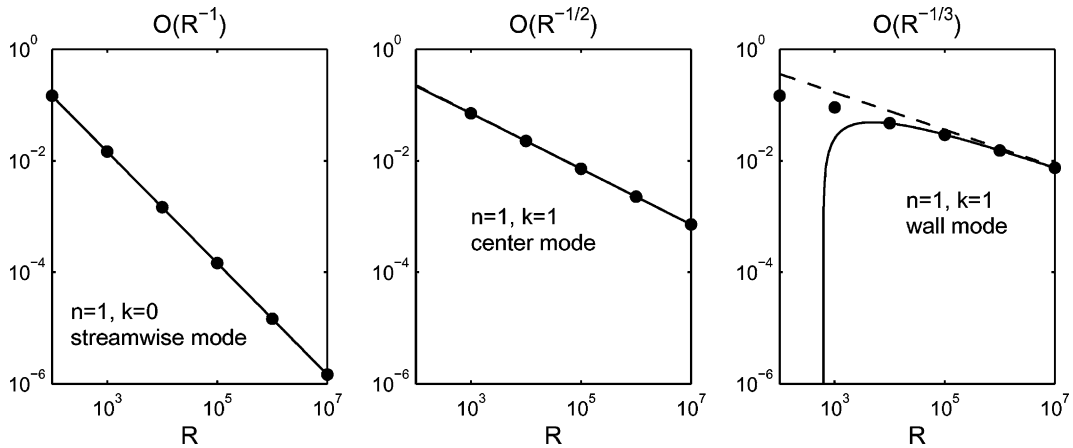
Fig. 3. (Negatives of) real parts of rightmost eigenvalues as a function of R for $n = 1$, $k = 0$ (streamwise modes) and $n = 1$, $k = 1$ (center modes, wall modes). The solid curves show the approximations (31)–(33). The dashed curves in the second and third plots (barely visible in the second plot) correspond to just the first terms of these approximations.
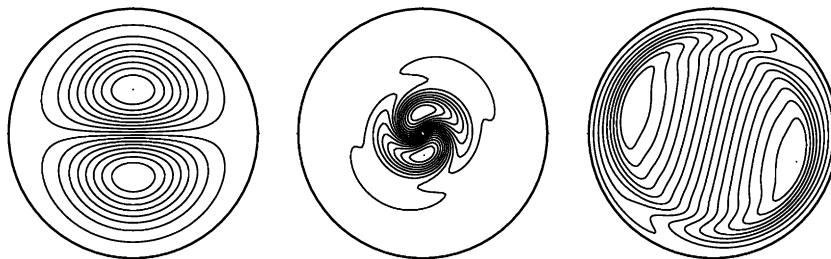

Fig. 4. Stream functions of the same three modes as in Fig. 3 for $R = 3000$. The angular orientation is arbitrary.

and for $k = 1$,

$$\sup_{t>0} \| \exp(t \mathcal{L}) \| \approx (R/0.565)^{1/3} - 5 \quad \text{attained at} \quad t \approx (R/1.15)^{1/3} + 6. \tag{35}$$

This formula has some significance for transition to turbulence, as will be discussed in next section.

Although wave numbers $k = 0$ and $k \neq 0$ behave differently, there must of course be a continuum connecting them. Fig. 7 gives some idea of how this works by comparing growth curves for $k = 0$, 0.03, 0.1, and 1, all for $n = 1$. At early times, a small wave number is not much different from $k = 0$. For large enough times, however, so long as k is nonzero, the relatively rapid decay appears; the time scale for values of k of order between R^{-1} and 1 is $R^{1/3}/k^{2/3}$. Fig. 8 gives further information about the differences between $k = 0$, where the "lift-up" mechanism of streamwise vortices generating streamwise streaks is relatively simple, and $k \neq 0$, where transient amplification involves more complicated time-dependent structures. For these flows t_{opt} scales as $R^{1/3}$, but the eventual decay of an optimal is on the longer time scale $R^{1/2}$, since as $t \to \infty$, the center modes whose eigenvalues have real part $O(R^{-1/2})$ must dominate.

The transient effects of Figs. 5–8 and Table 2 cannot be inferred from the eigenvalues of the operators in question, which are all in the left half-plane. However, they can be inferred from their
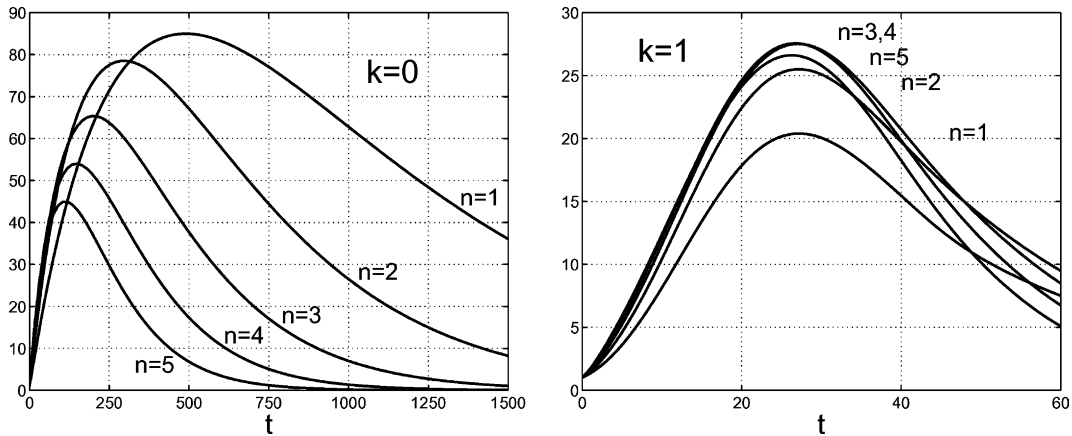
Fig. 5. $\| \exp(t\mathscr{L}) \|$ against t for $R = 10^4$ and $k = 0, 1$, various n. For $k = 0$, the growth is $O(R)$ on a time scale $O(R)$, while for $k \neq 0$ it is $O(R^{1/3})$ on a time scale $O(R^{1/3})$.
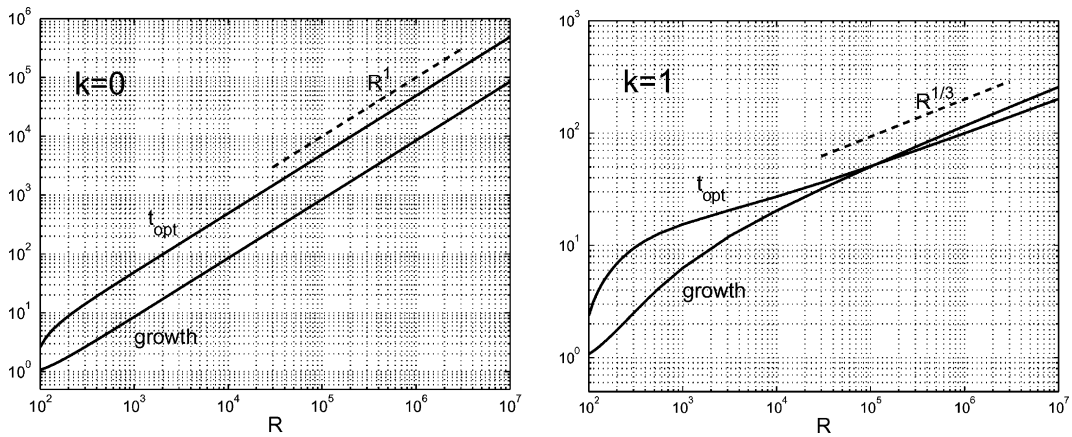

Fig. 6. Dependence of $\sup_t \| \exp(t\mathscr{L}) \|$ and t_{opt} on R for $n = 1$ and $k = 0, 1$.

Table 2
Transient growth factors and associated optimal times for $n = 1$ and $k = 0, 1$

R	$k = 0$	t_{opt}	$k = 1$	t_{opt}
10^2	1.066	2.578	1.068	2.344
10^3	8.510	48.78	6.275	15.39
10^4	84.92	489.7	20.40	27.18
10^5	849.2	4897.	50.22	50.80
10^6	8492.	48967	115.6	100.0
10^7	84919	489675	253.4	190.5

pseudospectra. For any matrix A and $\epsilon > 0$, the ϵ-pseudospectrum of A is the set of complex numbers z for which $\|(zI - A)^{-1}\| \geqslant \epsilon^{-1}$, or equivalently, the set of complex numbers z which are eigenvalues of $A + E$ for some perturbation matrix E with $\|E\| \leqslant \epsilon$ [10,30]. For linear operators, the definitions are the
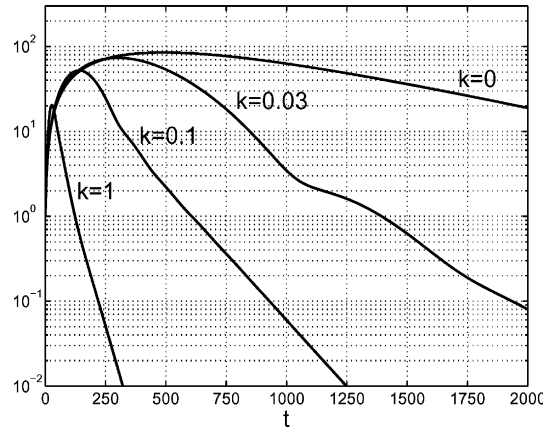
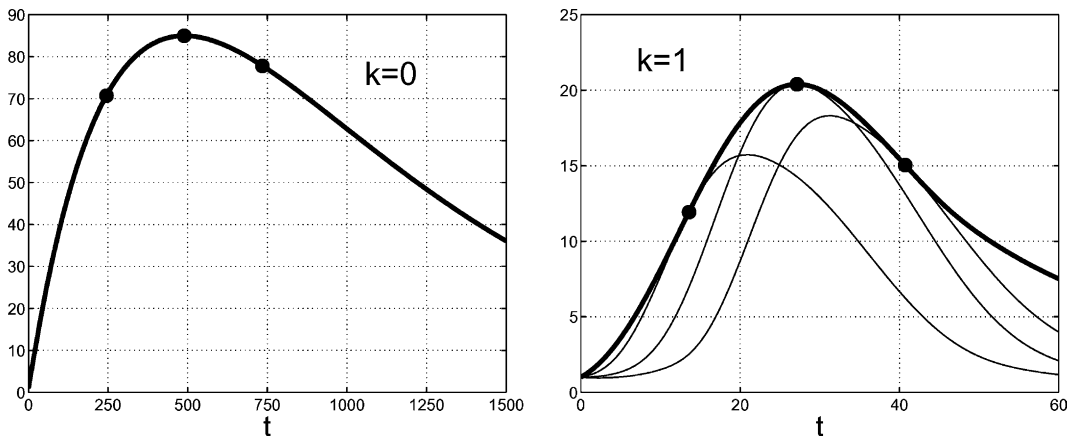Fig. 7. Transition from zero to nonzero wave numbers for $R = 10^4$, $n = 1$.

Fig. 8. Again for $R = 10^4$ and $n = 1$, the heavy curve shows the operator norm $\| \exp(t\mathscr{L})\|$, while the light curves show $\| \exp(t\mathscr{L})v\|$ for particular "optimals" chosen to achieve maximum amplification at t_{opt}, $0.5t_{opt}$, and $1.5t_{opt}$. For $k = 0$ the optimals are independent of t; the light curves are the same as the heavy one. For $k = 1$, however, an initial condition that maximizes growth at one time does not do so at others.

same apart from technicalities. Fig. 9 shows pseudospectra for linearized pipe flow operators with $R = 10^4$, computed with the aid of Wright's Eigtool package in MATLAB [34], (Figures like these have appeared previously in [27].) One sees immediately why the mathematically incorrect eigenvalues in the sixth plot of Fig. 1 took the form they did; note that that figure corresponded to $R = 10^5$, for which the pseudospectra look much as in Fig. 9 but for even smaller values of ϵ. In [31], three physical implications of pseudospectra are explored: transient growth, pseudoresonance, and susceptibility to destabilizing perturbations.

The most basic role of plots of pseudospectra is to alert one to situations in which eigenvalues are likely to be of limited physical significance. In addition, however, pseudospectra can lead to quantitative bounds. For example, a lower bound on transient growth can be derived by the Laplace transform [31]. For each ϵ, let $\alpha_\epsilon(\mathscr{L})$ be the ϵ-pseudospectral abscissa of $\mathscr{L}$, that is, the largest real part of an ϵ-pseudo-eigenvalue of
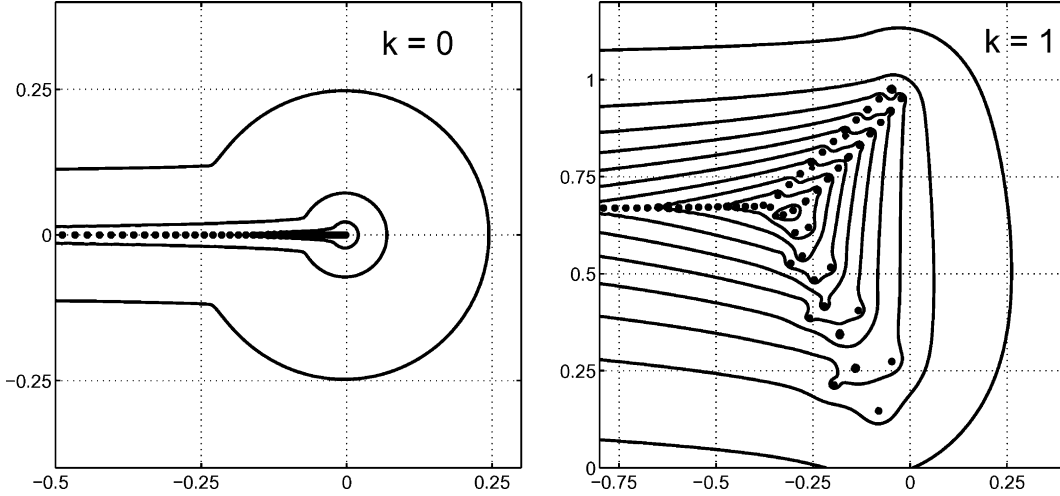
Fig. 9. Boundaries of ϵ-pseudospectra of the linearized pipe flow operator for $R = 10^4$, $n = 1$, and $k = 0$ and 1. From outside in, the curves correspond to $\epsilon = 10^{-1}$, $10^{-2}, \ldots, 10^{-10}$; only the first three are visible in the first figure. The second figure shows more striking nonnormality: the eigenvalues at the center of the "Y" are so ill-conditioned as to be physically meaningless, a phenomenon first identified for channel flows in [25]. It is the pseudospectra in the first figure that protrude more significantly into the right half-plane, however, causing larger transient growth.

$\mathscr{L}$. From the Laplace transform it can be deduced that for some t, $\|\exp(t\mathscr{L})\|$ must be at least as large as $\epsilon \alpha_\epsilon(\mathscr{L})$. Since this is true for each ϵ, we can take the supremum to obtain

$$\sup_{t>0}\|\exp(t\mathscr{L})\| \geqslant \sup_{\epsilon>0}\epsilon\alpha_\epsilon(\mathscr{L}). \tag{36}$$

For the pipe flow operator with $k = 0$, $n = 1$ we find

$$\sup_{t>0}\|\exp(t\mathscr{L})\| \geqslant R/170.96, \tag{37}$$

a lower bound which is 69% of the true maximum of (34). The point z_{opt} on the positive real axis corresponding to the optimal ϵ in (36) is $z_{\mathrm{opt}} \approx (R/20.11)^{-1}$.

From (31) and (32) we know that the distance of the rightmost eigenvalue from the imaginary axis scales for pipe flow with $n = 1$ as R^{-1} for $k = 0$ and $R^{-1/2}$ for $k = 1$. If these operators were normal, this would imply that the maximum resolvent norm along the imaginary axis scaled like R^1 and $R^{1/2}$, respectively. Infact, we find for $k = 0$

$$\sup_{s}\|(\mathscr{L} - \mathrm{i}sI)^{-1}\| \approx (R/28.89)^2 + (R^{3/2}) \quad \text{attained at } s = 0, \tag{38}$$

which is consistent with Eq. (7) of [32]. This number implies that the receptivity of pipe flow to external disturbances at low frequency is of order $\mathrm{O}(R^2)$: a small vibration of the right form could induce a much larger response.

7. Transition to turbulence

Transition to turbulence, like turbulence itself, depends on nonlinearity. Nevertheless, some insight into the process can be obtained from the linearized problem. We shall make two observations in this direction.

The first is presented in Fig. 10. As mentioned in Section 1, there are three classic examples of shear flows in which nonmodal transition has been most investigated: plane Poiseuille, plane Couette, and pipe flow. In [31], a figure was presented based on analysis of linearized plane Poiseuille and Couette flows. Here, we extend that figure to include a curve for pipe flow also, based on (38). Since $\|\mathcal{L}^{-1}\| \approx (R/28.89)^2$, the point $z = 0$ is on the boundary of the ϵ-pseudospectrum of $\mathcal{L}$ for $\epsilon \approx (28.89/R)^2$. For example, we have $\epsilon \approx 8.3 \times 10^{-6}$ for $R = 10^4$. This implies that although $\mathcal{L}$ itself is eigenvalue stable, there is an operator $\mathcal{E}$ with $\|\mathcal{E}\| < 10^{-5}$ for which $L + \mathcal{E}$ is unstable. As R increases, the norm of this minimal destabilizing perturbation shrinks quadratically.

Fig. 10 plots this relationship for pipe flow as well as the other two flows. (Since plane Poiseuille flow has an eigenvalue instability at $R \approx 5772$, the plane Poiseuille curve falls to $-\infty$ there.) On top of these curves are superimposed points corresponding to Reynolds numbers at which transition may be observed in practice ($R \approx 350$ for plane Couette, $R \approx 1000$ for plane Poiseuille, and $R \approx 2000$ for pipe flow). It is highly suggestive that all three dots appear at roughly the same height. Evidently transition becomes a possibility in all three of these flows at a Reynolds number where the minimal destabilizing perturbation is of a size between 10^{-4} and 10^{-3}. This is one of many similarities between these three flows.

This rough match between $\|\mathcal{L}^{-1}\|$ and transition should be taken as suggestive only. It is not clear that the irregularities of an actual flow experiment can be modeled in any precise way by a linear operator perturbation. Moreover, we are dealing with the low end of Reynolds numbers at which turbulence may appear, and the details of the nonlinear interactions in these three flows could in principle have had a decisive effect, making the results for the three flows differ strongly. Evidently this did not happen.

Our second observation about transition is rooted in a remarkable paper recently published by Chapman [6]. Going far beyond the caricature ODE models of transition presented in such papers as [1,11,31], Chapman performs an asymptotic analysis of the Navier–Stokes equations for plane Couette and plane Poiseuille flows and reaches conclusions about routes to transition. A central question is, what is the smallest-norm velocity perturbation of the ideal laminar flow that can excite transition, and in a scaling R^γ of this norm as $R \to \infty$, what is γ? The problem of determining this *threshold exponent γ* was posed in [31], where it was conjectured that for flows of this kind. $\gamma < -1$. Chapman argues that $\gamma = -3/2$ for plane Poiseuille flow and $\gamma = -1$ for plane Couette flow, even though numerical experiments have suggested $\gamma \approx -7/4$ in both cases [17,24,28].
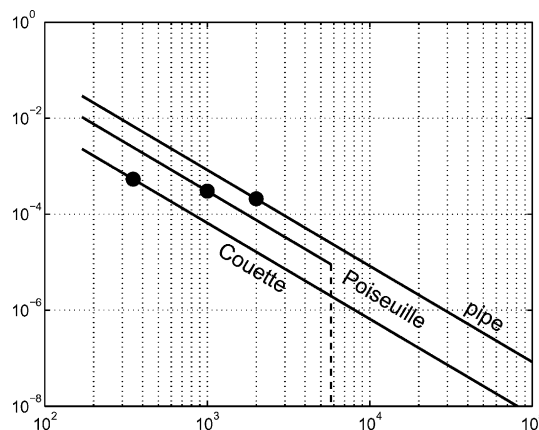

Fig. 10. Minimal norm of an operator perturbation that can destabilize a plane Couette, plane Poiseuille, or pipe flow, as a function of R. The dots mark the approximate lower Reynolds numbers at which transition to turbulence may be observed, and it is notable that they all lie at approximately the same height. (After Fig. 8 of [31].)

Thus Chapman concludes that the exponent γ observed in practice is different from the theoretically correct value. Moreover, he puts forward an explanation for this discrepancy. Let us define

$$f(R) = \log\left(\sup_{t>0}\|\exp(t\mathscr{L})\|\right), \tag{39}$$

where $\mathscr{L}$ is the linearized Navier–Stokes operator for the given Reynolds number R and a fixed set of nonzero Fourier parameters. The key point, Chapman argues, is that $f(R)$ curves downward as a function of R. Because of this curvature, the slope of $f(R)$ for values of R in the "laboratory" range 10^3–10^4 is greater than its asymptotic slope as $R \to \infty$. Chapman shows how this single phenomenon feeds through the various interactions to give an apparent γ for physical or numerical experiments that is significantly more negative than the true value.

Our computations for the pipe confirm Chapman's observations for channels. The function $f(R)$ appears in the second panel of Fig. 6, and it does indeed curve downward. The reason was encapsulated in (35),

$$\sup_{t>0}\|\exp(t\mathscr{L})\| \approx (R/0.565)^{1/3} - 5 + \mathrm{O}(R^{-1/3}). \tag{40}$$

This modest shift by about 5, entirely unremarkable from the general standpoint of asymptotics, can be expected to make the apparent threshold exponent derived from pipe observations for $R < 10^4$ significantly different from what would be found for $R \gg 10^6$. Chapman believes that the correct exponent is $\gamma = -1$ for pipe flow as for plane Couette flow (private communication), and nothing in our computations is inconsistent with that view.

8. Conclusion

In this paper we have proposed a new high-accuracy solenoidal Petrov–Galerkin spectral method for the discretization of the linearized Navier–Stokes equations in an infinite circular pipe, with a MATLAB implementation of this method given as a brief Appendix A. We have presented a range of computational results that significantly extend what has been obtained before, focusing especially on quantities related to nonmodal transient growth with azimuthal wave number $n = 1$ and axial wave numbers $k = 0$ and $k = 1$. These results go up to Reynolds number $R = 10^7$, enabling us to obtain asymptotic expressions as $R \to \infty$ for a number of quantities including eigenvalue locations, transient growth amplitude, transient growth time, and resolvent norms. Some of these asymptotic results are summarized in Table 3. Similar tables of results for plane Couette and plane Poiseuille flows have appeared in [31].

Although the results presented here are all linear, they shed light on the nonlinear problem of transition to turbulence. In particular we find that the transient growth of nonstreamwise ($k \neq 0$) modes approaches

Table 3
Summary of asymptotic results as $R \to \infty$ (all attained with $k = 0$, $n = 1$)

Distance of spectrum from imag. axis	$(R/14.68)^{-1}$
$\|\mathscr{L}^{-1}\|$	$(R/28.89)^2$
$\sup_{t>0}\|\exp(t\mathscr{L})\|$	$R/117.7$
t_{opt} for above	$R/20.42$
Lower bound based on pseudospectra	$R/171.0$
z_{opt} for above	$(R/20.11)^{-1}$

its $R \to \infty$ asymptote slowly, as has been found by Chapman for channel flows [6], implying that one may expect the apparent threshold exponent γ for transition obtained from numerical or physical experiments in the "laboratory" range of Reynolds numbers 10^3–10^4 to be more negative than its true asymptotic value as $R \to \infty$.

Our linear code has been extended to a fully nonlinear code for direct numerical solution of the Navier–Stokes equations. For initial results from our nonlinear simulations, see [19].

Acknowledgements

Appendix A. MATLAB CODE

```
function [r,A,B] = pipe(Re,n,k,M)

% SPECTRAL CODE FOR ANALYSIS OF LINEARIZED IDEAL PIPE FLOW
%
% A. Meseguer and L. N. Trefethen, Oxford University, 2001.
% See "Linearized pipe flow to Reynolds number 10^7"
% and http://web.comlab.ox.ac.uk/oucl/work/nick.trefethen.
%
% Inputs:
% Re = Reynolds number
% n  = azimuthal wavenumber (integer)
% k  = axial wavenumber (real)
% M  = number of Chebyshev modes for radial approximation
%
% Outputs:
% r = Chebyshev grid in radial direction
% A, B = matrices defining evolution problem B*(du/dt) = A*u

% Weak formulation:
% The evolution equation for given wavenumbers n and k is
% (w,v_t) = (w,Lv) for all solenoidal test functions w, with inner product
% (f,g) = int_0^1 f*(r) g(r) r dr.   L = L(n,k) is the Navier-Stokes
% operator linearized about laminar flow, with pressure terms omitted
% since they drop out in the inner product.

% Petrov-Galerkin numerical method:
% v and w are taken from finite-dimensional spaces constructed from
% Chebyshev polynomials; the basis vectors are stored as columns of
% a matrix V and as rows of a matrix W (pre-scaled by r/sqrt(1-r^2)).
% Inner product integrals are carried out by Chebyshev-Gauss-Lobatto
% quadrature on a grid fine enough to give exact results for the
% given basis functions.

% Internal variables:
%     rr = quadrature points in [-1,1] for quadrature
%      r = restriction of rr to (0,1)
%      D = Chebyshev differentiation matrix
%  DE,DO = even and odd halves of D, or reverse if n is odd
% D2E,D2O = likewise for D^2
```

```
% Initializations:
  global DE D0
  N = 2*M+7;            % number of grid points in (-1,1]
  K = (N-1)/2;          % number of grid points in (0,1)
  half = 2:K+1;         % indices of grid points in (0,1)
  rad = 1:K;            % indices of radial components of V & W
  az = K + rad;         % indices of azimuthal components
  ax = K + az;          % indices of axial components
% Chebyshev mesh and differentiation matrix for rr in [-1,1]
% (see cheb.m in chap. 6 of Trefethen, Spectral Methods in Matlab):
  rr = cos(pi*(0:N)/N)';
  c = [2; ones(N-1,1); 2].*(-1).^(0:N)';
  X = repmat(rr,1,N+1);
  dX = X-X';
  D = (c*(1./c)')./(dX+(eye(N+1)));     % off-diagonal entries
  D = D - diag(sum(D'));                % diagonal entries
% Extraction from D and D^2 of pieces corresponding to r in (0,1)
% (see chap. 11 of Trefethen, Spectral Methods in Matlab):
  r = rr(half);
  s = (-1)^mod(n,2);
  DE = D(half,half) + s*D(half,N+2-half);
  D0 = D(half,half) - s*D(half,N+2-half);
  D2 = D(half,:)*D;
  D2E = D2(:,half) + s*D2(:,N+2-half);
  D20 = D2(:,half) - s*D2(:,N+2-half);
% Computation of solenoidal basis and dual basis:
  V = zeros(3*K,2*M+2); W = zeros(2*M+2,3*K);
  for m = 0:M
    p = [m+1 m+M+2];
    V(:,p) =      basis(n,k,r,m);
    W(p,:) = dualbasis(n,k,r,m);
  end
% Linearized Navier-Stokes operator (eqs. (20)-(22) of paper):
  I = speye(K);              % 1
  R = spdiags(r,0,K,K);      % r
  Ri = spdiags(1./r,0,K,K);       % r^(-1)
  Ri2 = spdiags(1./r.^2,0,K,K);   % r^(-2)
  Lam = (I-R.^2); dLam = -2*R;    % laminar profile and its gradient
  LV = zeros(3*K,2*M+2);
  TMP = -n^2*Ri2 - k^2*I + i*k*Re*Lam;
  LV(rad,:) = (D20 + Ri*D0 - Ri2 + TMP)*V(rad,:) - 2i*n*Ri2*V(az,:);
  LV( az,:) = (D20 + Ri*D0 - Ri2 + TMP)*V( az,:) + 2i*n*Ri2*V(rad,:);
  LV( ax,:) = (D2E + Ri*DE      + TMP)*V( ax,:) + Re*dLam*V(rad,:);
  LV = LV/Re;
  B = W*V;
  A = W*LV;

function V = basis(n,k,r,m)

  global DE D0
  zero = zeros(size(r));
  an = min(abs(n),2-mod(n,2));
  h = (1-r.^2).*cos(2*m*acos(r)); g = (1-r.^2).*h;

  if n==0
    u1=zero;                   u2=-i*k*r.*g;
    v1=r.*h;                   v2=zero;
    w1=zero;                   w2=D0*(r.*g)+g;
  else
    u1=-i*n*r.^(an-1).*g;      u2=zero;
    v1=DE*(r.^an.*g);          v2=-i*k*r.^(an+1).*h;
    w1=zero;                   w2=i*n*r.^an.*h;
  end
```

```
  if k==0 & n==0, w2=h; end
  V = [u1 u2; v1 v2; w1 w2];

function W = dualbasis(n,k,r,m)

% Generates dual basis as two row vectors, already complex conjugated.
% The factors 1/sqrt(1-r^2) are omitted, as these cancel in Gauss
% quadrature, but the factor (pi*r)/N needed in quadrature is included.

  global DE DO
  zero = zeros(size(r));
  h = (1-r.^2).*cos(2*m*acos(r)); g = (1-r.^2).*h;

  if n==0
    u1=zero;                      u2=i*k*r.^2.*g;
    v1=h;                         v2=zero;
    w1=zero;                      w2=DE*(r.^2.*g)+r.^3.*h+r.*g;
  else
    s = mod(n,2);
    u1=i*n*g.*r.^s;               u2=zero;
    v1=DO*(g.*r.^(s+1))+r.^(s+2).*h;  v2=-i*k*r.^(s+2).*h;
    w1=zero;                      w2=i*n*r.^(s+1).*h;
  end

  if k==0 & mod(n,2)==1, w2 = i*n*h; end
  if k==0 & n==0, w2 = r.*h; end
  N = 2*(length(r)+1);
  W  = ((pi/N)*[r r; r r; r r].*[u1 u2; v1 v2; w1 w2]).';

function L = makeL(n,k,A,B,M)

% Converts A and B to energy weighted matrix L = B\A.  This conversion
% is not needed for linear or nonlinear simulations, only for subsequent
% analysis of results.  Gauss-Legendre quadrature has accordingly been
% used for simplicity, although alternative approaches would be possible.

  [V,E] = eig(A,B);
  [tmp,ii] = sort(real(diag(E)));
  V = V(:,ii); E = E(ii,ii);
  [x,w,D] = gauss_legendre(2*M+7);
  r = (x+1)/2; D = 2*D;
  for m=1:M+1
    VP(:,[m m+M+1]) = basisD(n,k,r,m,D);
  end
  wr = sparse(sqrt(w.*r'));
  F = (1/sqrt(2))*diag([wr wr wr])*VP*V;
  [Q,R] = qr(F,0);
  L = R*E/R;

function v = basisD(n,k,r,m,D)   % like basis.m, but for arbitrary diff. mat. D

  zero = zeros(size(r));
  an = min(abs(n),2-mod(n,2));
  h = (1-r.^2).*cos(2*(m-1)*acos(r)); g = (1-r.^2).*h;

  if n==0
    u1=zero;                      u2=-i*k*r.*g;
    v1=r.*h;                      v2=zero;
    w1=zero;                      w2=D*(r.*g)+g;
  else
    u1=-i*n*r.^(an-1).*g;         u2=zero;
    v1=D*(r.^an.*g);              v2=-i*k*r.^(an+1).*h;
    w1=zero;                      w2=i*n*r.^an.*h;
  end

  if k==0 & n==0, w2=h; end
  v = [u1 u2; v1 v2; w1 w2];

function [x,w,D] = gauss_legendre(N)   % Gauss-Legendre points, weights,
                                       % and spectral differentiation matrix
```

```
% Points and weights (see chap. 12 of Trefethen, Spectral Methods in MATLAB):
  beta = .5./sqrt(1-(2*(1:N-1)).^(-2));
  T = diag(beta,1) + diag(beta,-1);
  [V,D] = eig(T);
  x = diag(D); [x,i] = sort(x);
  w = 2*V(1,:).^2;

% Differentiation matrix (see chap. 8 of same book):
  ii = (1:N)';
  q = zeros(N,1); D = zeros(N,N);
  for i = 1:N, q(i) = prod(x(i)-x(find(ii~=i))); end
  H = diag((x-1).*q);
  for j = 1:N
    tmp = x(ii)-x(j); tmp(j) = x(j)^2-1; D(:,j) = 1./tmp;
  end
  D = H*D/H;
```

References

[1] J.S. Baggett, L.N. Trefethen, Low-dimensional models of subcritical transition to turbulence, Phys. Fluids 9 (1997) 1043.
[2] L. Bergström, Optimal growth of small disturbances in pipe Poiseuille flow, Phys. Fluids A 11 (1993) 2710.
[3] L. Boberg, U. Brosa, Onset of turbulence in a pipe, Z. Naturforsch. 43a (1988) 696.
[4] K.M. Butler, B.F. Farrell, Three-dimensional optimal perturbations in viscous shear flow, Phys. Fluids A 4 (1992) 1637.
[5] C. Canuto, M.Y. Hussaini, A. Quarteroni, T.A. Zang, Spectral Methods in Fluid Dynamics, Springer, New York, 1988.
[6] S.J. Chapman, Subcritical transition in channel flows, J. Fluid Mech. 451 (2002) 35.
[7] A.G. Darbyshire, T. Mullin, Transition to turbulence in constant mass-flux pipe flow, J. Fluid Mech. 289 (1995) 83.
[8] A.A. Draad, G.D.C. Kuiken, F.T.M. Nieuwstadt, Laminar-turbulent transition in pipe flow for Newtonian and non-Newtonian fluids, J. Fluid Mech. 377 (1998) 267.
[9] P.G. Drazin, W.H. Reid, Hydrodynamic Stability, Cambridge University Press, Cambridge, 1981.
[10] M. Embree, L.N. Trefethen, Pseudospectra Gateway, web site at http://www.comlab.ox.ac.uk/pseudospectra.
[11] T. Gebhardt, S. Grossmann, Chaos transition despite linear stability, Phys. Rev. E 50 (1994) 3705.
[12] L.H. Gustavsson, Energy growth of three-dimensional disturbances in plane Poiseuille flow, J. Fluid Mech. 224 (1991) 241.
[13] J. Komminaho, A.V. Johansson, Development of a spectrally accurate DNS code for cylindrical geometries, part V of J. Komminaho, Direct Numerical Simulation of Turbulent Flow in Plane and Cylindrical Geometries, Doctoral Thesis, Royal Institute of Technology, Stockholm, 2000.
[14] G. Kreiss, A. Lundbladh, D.S. Henningson, Bounds for threshold amplitudes in subcritical shear flows, J. Fluid Mech. 270 (1994) 175.
[15] L.D. Landau, E.M. Lifshitz, Fluid Mechanics, Pergamon Press, Oxford, 1959.
[16] A. Leonard, A. Wray, A new numerical method for the simulation of three dimensional flow in a pipe, in: E. Krause (Ed.), Proceedings of the 8th International Conference on Numerical Methods in Fluid Dynamics, Springer, Berlin, 1982.
[17] A. Lundbladh, D.S. Henningson, S.C. Reddy, Threshold amplitudes for transition in channel flows, in: Transition, Turbulence and Combustion, vol. I, Kluwer Academic Publishers, Dordrecht, 1994.
[18] Á. Meseguer and L.N. Trefethen, A spectral Petrov–Galerkin formulation for pipe flow I: linear stability and transient growth, Rep. 00/18, Numerical Analysis Group, Oxford University, Computing Lab., 2000, available at http://web.comlab.ox.ac.uk/oucl/publications/natr/.
[19] Á. Meseguer, L.N. Trefethen, A spectral Petrov–Galerkin formulation for pipe flow II: nonlinear transitional stages, Rep. 01/19, Numerical Analysis Group, Oxford University, Computing Lab., 2001, available at http://web.comlab.ox.ac.uk/oucl/piiblications/natr/.
[20] R.D. Moser, P. Moin, A. Leonard, A spectral numerical method for the Navier–Stokes equations with applications to Taylor–Couette flow, J. Comp. Phys. 52 (1983) 524.
[21] P.L. O'Sullivan, K.S. Breuer, Transient growth in a circular pipe. I. Linear disturbances, Phys. Fluids 6 (1994) 3643.
[22] V.G. Priymak, T. Miyazaki, Accurate Navier–Stokes investigation of transitional and turbulent flows in a circular pipe, J. Comp. Phys. 142 (1998) 370.
[23] S.C. Reddy, D.S. Henningson, Energy growth in viscous channel flows, J. Fluid Mech. 252 (1993) 209.
[24] S.C. Reddy, P.J. Schmid, J.S. Baggett, D.S. Henningson, On stability of streamwise streaks and transition thresholds in plane channel flows, J. Fluid Mech. 365 (1998) 269.

[25] S.C. Reddy, P.J. Schmid, D.S. Henningson, Pseudospectra of the Orr–Sommerfeld operator, SIAM J. Appl. Math. 53 (1993) 15.
[26] O. Reynolds, An experimental investigation of the circumstances which determine whether the motion of water shall be direct or sinuous, and of the law of resistance in parallel channels, Philos. Trans. Roy. Soc. 174 (1883) 935.
[27] P.J. Schmid, D.S. Henningson, Optimal energy growth in Hagen–Poiseuille flow, J. Fluid Mech. 277 (1994) 197.
[28] P.J. Schmid, D.S. Henningson, Stability and Transition in Shear Flows, Springer, New York, 2001.
[29] H. Shan, B. Ma, Z. Zhang, F.T.M. Nieuwstadt, Direct numerical simulation of a puff and a slug in transitional cylindrical pipe flow, J. Fluid Mech. 387 (1999) 39.
[30] L.N. Trefethen, Pseudospectra of linear operators, SIAM Rev. 39 (1999) 247.
[31] L.N. Trefethen, A.E. Trefethen, S.C. Reddy, T.A. Driscoll, Hydrodynamic stability without eigenvalues, Science 261 (1993) 578.
[32] A.E. Trefethen, L.N. Trefethen, P.J. Schmid, Spectra and pseudospectra for pipe Poiseuille flow, Comp. Meth. Appl. Mech. Eng. 1926 (1999) 413.
[33] L.S. Tuckerman, Divergence-free velocity fields in nonperiodic geometries, J. Comp. Phys. 80 (1989) 403.
[34] T.G. Wright, Eigtool (MATLAB software package), available at http://www.comlab.ox.ac.uk/pseudospectra/eigtool/.
[35] I.J. Wygnanski, F.H. Champagne, On transition in a pipe. Part 1. The origin of puffs and slugs and the flow in a turbulent slug, J. Fluid Mech. 59 (1973) 281.
[36] Y. Zhang, A. Gandhi, A.G. Tomboulides, S.A. Orszag, Simulation of pipe flow, in: Application of Direct and Large Eddy Simulation to Transition and Turbulence, AGARD Conference, Crete, 1994, pp. 17.1–17.9.
[37] O.Yu. Zikanov, On the instability of pipe Poiseuille flow, Phys. Fluids 8 (1996) 2923.